CrossMark

# Development of a collinear laser spectrometer facility at VECC: First test result

MD SABIR ALI[1,*], AYAN RAY[1], WASEEM RAJA[2], ARUP BANDYOPADHYAY[3], VAISHALI NAIK[1], ASISH POLLEY[3] and ALOK CHAKRABARTI[1]

[1]Radioactive Ion Beam Group, Variable Energy Cyclotron Centre, Kolkata 700 064, India
[2]Department of Physics, University of Kashmir, Srinagar 190 006, India
[3]Accelerator Physics Group, Variable Energy Cyclotron Centre, Kolkata 700 064, India
*Corresponding author. E-mail: sabirbarc@gmail.com

**Abstract.** We report here the development of collinear laser spectroscopy (CLS) system at VECC for the study of hyperfine spectrum and isotopic shift of stable and unstable isotopes. The facility is first of its kind in the country allowing measurement of hyperfine splitting of atomic levels using atomic beams. The CLS system is installed downstream of the focal plane of the existing isotope separator online (ISOL) facility at VECC and is recently commissioned by successfully resolving the fluorescence spectrum of the hyperfine levels in $^{85,87}$Rb. The atomic beams of Rb were produced by charge exchange of 8 keV Rb ion beam which were produced, extracted and transported to the charge exchange cell using the ion sources, extractor and the beam-line magnets of the ISOL facility. The laser propagating opposite to the ion/atom beam direction was allowed to interact with the atom beam and fluorescence spectrum was recorded. The experimental set-up and the experiment conducted are reported in detail. The measures needed to be carried out for improving the sensitivity to a level necessary for studying short-lived exotic nuclei have also been discussed.

**Keywords.** Collinear laser spectrometer; isotope separator online; charge exchange; ellipsoid reflector; photon counting.

**PACS Nos** 21.10.−K; 27.50.+e; 42.62.Fi

## 1. Introduction

The high degree of coherence of laser light paves the way for doing spectroscopy with fast ion/atom beams. This technique has been known as fast ion beam laser spectroscopy (FIBLAS) [1]. This was proposed by Kaufman [2] and independently by Wing *et al* [3]. Experimental realisation of the same has been reported first by Anton *et al* [4]. The same technique, with further modification, which is commonly known as collinear laser spectroscopy (CLS) [5–8] in its current form, is used in the field of rare ion beam (RIB) research to extract valuable nuclear data (magnetic dipole moment, electric quadrupole moment, isotope shift, charge radius etc. of exotic nuclei) in a model-independent way [5,6]. More precisely, CLS is used as a workhorse to study the most poorly explored or undiscovered nuclear species located on the neutron-rich side of the nuclear chart, forming the *terra incognita* for nuclear structure investigations

[7–9]. In due course it has become an integral part of the RIB facilities worldwide, such as ISOLDE CERN, NSCL MSU, ISAC TRIUMF, IGISOL JYFL etc. [10]. A recent review on current measurements, advances at facilities and the future direction of the field may be found in ref. [10] and the references therein.

In this report, we describe the ongoing development of a CLS set-up in Variable Energy Cyclotron Centre (VECC) under the umbrella of the ongoing RIB project. The prototype has been used with an existing isotope separator online (ISOL) system [11] and is commissioned offline by successfully resolving the fluorescence spectra of $^{85,87}$Rb atom beams. In the first stage, the $^{85}$Rb$^+$,$^{87}$Rb$^+$ ions are produced in a surface ionisation (SI) source, transported and mass-separated. The mass-separated beam is further charge-converted to generate respective atom beam. The laser beam counterpropagates the atom beam in the present set-up. An ellipsoid reflector is used in the atom–laser interaction

path to enable efficient guiding of fluorescence photons to a photomultiplier tube (PMT). Fluorescence spectrum is detected by using synchronous/chopped photon counting method. The following sections describe the essentials of the CLS beam line, photon counting system (PCS) and results obtained so far. Based on these results, the sensitivity of the system is evaluated and it is being upgraded further to detect rare atomic species. Initially $^{42}K^+$, $^{43}K^+$ are chosen as the stepping stones as these elements are well-studied RIB species [12] and they have been generated and successfully transported earlier by our group [13,14].

## 2. Atomic hyperfine structure and laser nuclear spectroscopy

The hyperfine interaction energy of a state with hyperfine quantum number $F$, total angular momentum quantum number $J$ and nuclear spin $I$ is given by [5,6]

$$W(F) = \frac{AK}{2} + B\frac{\frac{3}{2}K(K+1) - 2I(I+1)J(J+1)}{4I(2I-1)J(2J-1)}.$$

(1)

Here $K = F(F+1) - I(I+1) - J(J+1)$, $A = g\mu_N B(0)\hbar/\vec{I} \cdot \vec{J}$ and $B = eQ_s\phi_{jj}(0)$ are hyperfine constants, $\mu_N (Q_s)$ are the Bohr magneton (electric quadrupole) moment of the nucleus, $B(0)$ is the magnetic field generated at the nuclear site by electrons and $\phi_{jj}(0)$ is the electric field gradient produced by electrons at the nucleus. The hyperfine spectroscopy of an isotope chain reveals the isotope shift (IS) which has two components: mass shift and field shift. The nominal frequency for transition does not change under first-order perturbation theory, while the individual hyperfine components shift around it. The mass shift is an effect of atomic structure and the field shift appears due to the effect of finite extension of the nuclear charge distribution on the electronic binding energy. The field shift [5,6] provides an estimate of the change of nuclear charge radius within an isotopic series or between isomers. The ratio of field shifts and difference of mass shift factors can be obtained separately through King Plot [5]. In the case of CLS, the longitudinal velocity spread of the atoms is reduced due to acceleration cooling [1–3]. This results in the observation of high-resolution spectra and it becomes possible to extract with precision the information about the ground state of the nucleus.

## 3. The laser spectrometer beam line

The CLS beam line (figure 1) is connected to the existing ISOL beam line, which comprises a surface ion (SI) source and beam guiding optics (a set of two magnetic quadrupoles and a magnetic dipole) [11]. In the present experiment, commercial rubidium chloride salt (Sigma Aldrich) is used in very small quantity inside the cathode of the ion source to produce $Rb^+$ ions. The local vacuum of the total beam line is kept at $\sim 10^{-6}$ mbar. A Faraday cup (FC1) and a wire scanner are introduced at the end of the old beam line to record ion beam current and beam profile. Another Faraday cup (FC2) is used at the end of the charge exchange cell (CEC). The beam optics of the present set-up is simulated using the computer code TRANSPORT [15] and the simulated beam diameters are $X_{dia}(Y_{dia}) = 2.0$ cm (0.72 cm) at the start of CEC, $X_{dia}(Y_{dia}) = 1.34$ cm (0.59 cm) at FC2 and $X_{dia}(Y_{dia}) = 2.41$ cm (0.88 cm) at the reflector entry. The new CLS (see figure 1) beam line comprises five major parts.

### 3.1 *Charge exchange cell (CEC)*

A Rb ingot (Sigma Aldrich, 5 g ampoule) is used in the reservoir (see figure 2A). A mechanical feed-through arrangement is used to break the seal of the ingot under a vacuum level of $\sim 10^{-6}$ mbar. The reservoir is heated to maintain a gradient of 200°C (bottom of the reservoir) to $\sim 140$°C (the ion beam pass zone). Cooling tubes (circulating low conductivity water at 27°C) are brazed to the end parts of the ion beam pass zone (figure 2A) and flow rate ($\sim \leq 5$ l/min) is so adjusted that the temperature at the end faces drops to $\sim 50$°C, which is a few degrees above the melting point (39.3°C) for Rb. This condition helps in condensing [16,17] the hot Rb vapour into droplets, which stick to an embedded wick structure [16] and circulates back to the reservoir due to capillary action. Further, the inner side of the end parts of the ion beam pass zone is machined with a 6° tapering to utilise gravity for recirculation. In the current experiment, a 5-g ampoule is used for $\sim 25$ h of operation (with nearly constant efficiency) and it is still continuing. In order to have some idea about the CEC full operation time the system needs to be tested for several full cycles of CEC operation which is yet to be completed. Two ion pumps are used at both ends of the CEC pipe to remove leaked Rb vapour, if any, from the hot vacuum environment.

### 3.2 *Photon guiding (PG)*

The laser beam is superposed with the atom/ion beam over the full length up to the dipole magnet. An ellipsoid reflector (REM-144.2-31.8-21.0, CVI Melles Griot), which is 300 mm downstream from the end of the CEC, is used in the beam line (see figure 3). The reflector is specially machined to create circular
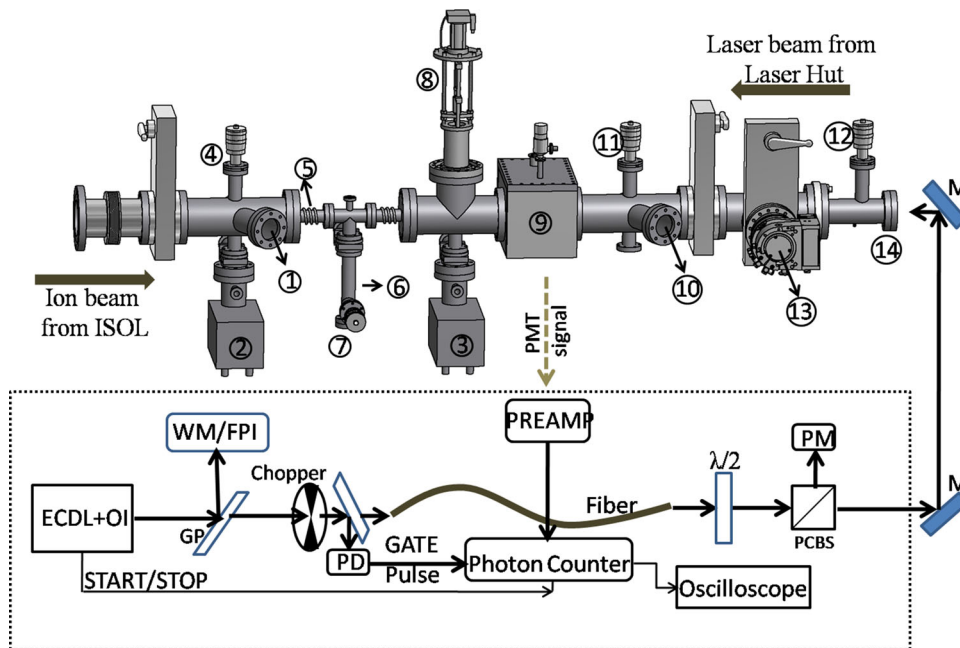
**Figure 1.** The CLS beam line with photon counting system (PCS). Here 1, 10: observation viewports; 2, 3: ion pumps; 4, 11, 12: feed-through assembly for laser beam alignment; 5: cooling tube for CEC; 6: alkali metal reservoir for CEC; 7: feed-through assembly for breaking the alkali break-seal ampoule; 8: Faraday cup; 9: photon guide box; 13: turbo pump; 14: laser beam entry viewport. The dotted section shows the schematic of PCS where ECDL: External cavity diode laser, OI: optical isolator, GP: glass plate, PD: photodiode, PREAMP: preamplifier, WM: wavemeter, FPI: Fabry Perot etalon marker, $\lambda/2$: half waveplate, PCBS: polarising cubic beam splitter, PM: power meter, M: mirror, PMT: photomultiplier tube (not shown).
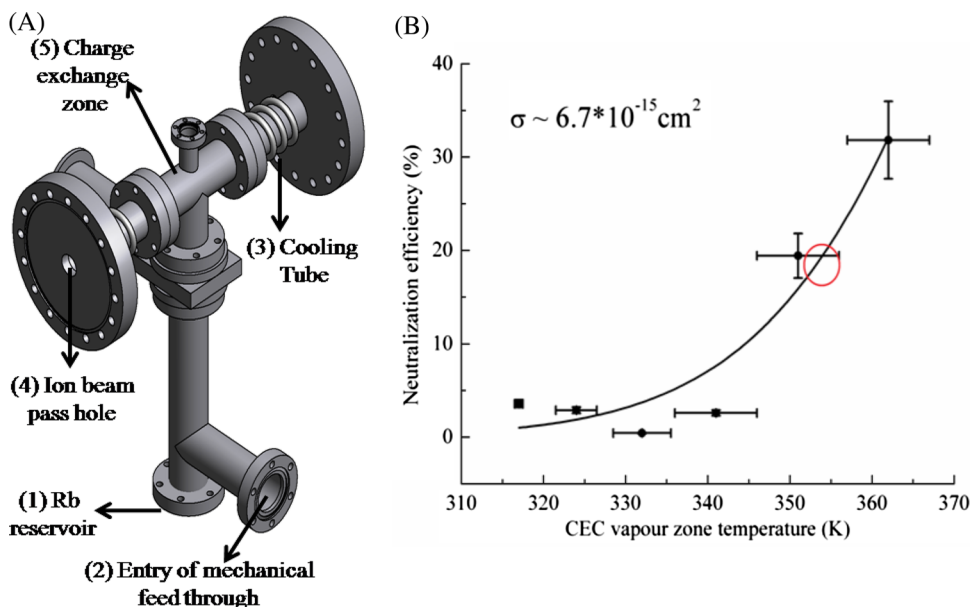


**Figure 2.** (**A**) The charge exchange cell is shown with all parts. (**B**) The CEC calibration curve is shown. The fitted cross-section is $\sigma \sim 6.7 * 10^{-15} \text{cm}^2$. Equations (3) and (4) are used for fitting purpose. The highlighted portion marks the operating zone. We used relatively lower neutralisation efficiency of $\sim$15–20% for the experiment. The data of saturation part of CEC are not used as this region may lead to multiple scattering and *vis à vis* higher emittance of the beam and is not of our interest.

holes (diameter = 30 mm) on the opposite surfaces. This is done to allow the ion/atom-laser beams traverse through the first focus. According to the ellipsoid geometry scattered photons from the primary focus will be directed to the secondary focus. The location of the secondary focus is just a few mm outside the fused silica
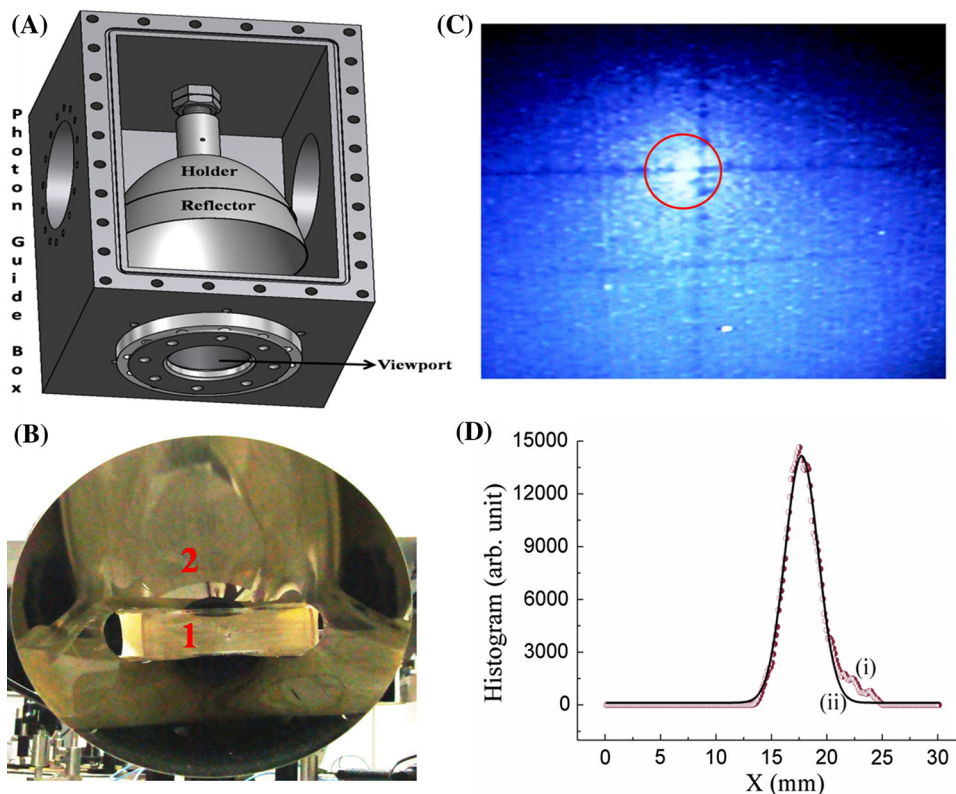
**Figure 3.** Offline calibration of the ellipsoid reflector. (**A**) 3D view of the photon guide box. The ellipsoid reflector is mounted to the mechanical holder (see text for details). (**B**) The Rb vapour cell is mounted along the first focus line of the ellipsoid reflector with the help of a PVC tube for offline calibration. The vapour cell is marked with no. 1 and PVCube is marked with no. 2. (**C**) shows the scattered light from the reflector on a screen when laser light is passed through the vapour cell under on-resonance. The highlighted portion shows the fluorescence intensity from the reflector when the laser is tuned on $^{85}$Rb $5^2S_{1/2}F = 3 \rightarrow 5^2P_{3/2}F'$ transition. (**D**) shows (i) the histogram of the highlighted portion of (**C**), and (ii) Gauss fitting is done to see that the fluorescence photons are mainly confined within an area of $\sim$10 mm$^2$.

viewport which isolates the beam line from outside. The reflector has rhodium coating on nickel base, which provides $\sim\geq$80% reflectance over 400 to 900 nm wavelength zone. It is mounted with Torrseal to the holder, which is again mechanically mounted to the body of the light guide box (figure 3A). The holder contains conical projections (light arrester) at the beam entry and exit ports. This particular geometry is chosen to reduce the effect of scattered photons from laser light. Further, thin black aluminum foil (BKF12, Thorlabs) is pasted on the inside surfaces of the PG box and its surroundings with Torrseal to arrest scattered photons.

### 3.3 *Laser section (LS)*

In the current design we worked with a counterpropagating geometry (figure 1). This is because the dipole magnet with the existing ISOL system [11] does not contain zero degree port to introduce the laser beam copropagating with the ion beam. Therefore, the light

beam (linearly polarised) from the external cavity diode laser (DL100 Pro, Toptica) is transported before the fused silica viewport (at the extreme end of the CLS beam line) by using a single-mode optical fibre. The intensity is varied by using $\lambda/2$ plate, polarising cubic beam splitter (PCBS) combinations. The fibre collimator helps to collimate the laser beam. Using the collimator holder, one additional mirror and few removable screens, the laser beam was aligned with the first focus. Starting from the laser entry port side, three removable screens (12, 11, 4 of figure 1) with graded axial strokes at three different positions are used for alignment purpose. A pair of side ports (at 45° projection; 1, 10 of figure 1) is used to view the laser beam spots on the removable screens. The laser beam has to pass through the middle of the narrow entries of two light arresters, CEC to be simultaneously seen on the first and the last screens. This condition ensures the alignment of the laser where the middle screen is used as the reference point for position adjustment. Similar exercise

is followed with ion beam where the beam current is measured at different points (especially Faraday cup at 8, end flange at 14 of figure 1; end flange is in floated condition). Thus, the superposition of laser-ion beam is ensured.

### 3.4 *The photon counting system (PCS)*

The PCS (figure 1) is centred on Hamamatsu R943-02 photomultiplier tube (PMT), which has a quantum efficiency (QE) of $\sim\geq 10\%$ over 400 to 800 nm wavelength region and mounted head-on to the viewport. It has an effective area of $\sim 100\,\text{mm}^2$. The output of the PMT is processed through a fast preamplifier (SR445A, Stanford Research) and the final counting is done with a SR400 gated photon counter. We used synchronous photon counting to eliminate background count due to stray light (other than counts due to scattering of laser light). For this purpose, a mechanical chopper (MC2000EC, Thorlabs) is used to generate bright/dark light states, which generates the trigger pulse. The A and B gates of the counters are kept open for a period less than that of the period of chopper to avoid the effect of chopper frequency drift or jitter from disturbing the gate/chopper overlap. The D/A output (corresponding to A-B of the counter), which is linearly proportional to the count data, is recorded. This is an existing PCS set-up in the lab for experiments related to quantum optics [18] and is also used in the same form for the first trial run of the spectrometer.

### 3.5 *Beam diagnostics*

Here FC1 is used to measure the beam current ($I_{\text{FC1}}$). The wire scanner (before FC1) is used to observe the beam profile, which helps in the optimisation of the same by tuning the beam optics elements. The FC2 measures the ion beam current ($I_{\text{FC2}}$) after CEC (see figure 1). The fraction $\eta = (1 - I/I_0)$ is the charge exchange efficiency of the CEC. $I_0$ is defined as $I_0 = I_{\text{FC2}}/I_{\text{FC1}}$ when CEC is OFF and $I = I_{\text{FC2}}/I_{\text{FC1}}$ when CEC is ON. The corresponding $I_{\text{FC2}}$ is normalised with respect to $I_{\text{FC1}}$ to take care of fluctuations in $I_{\text{FC2}}$ due to any reason other than charge exchange mechanism. This way the attenuation in $I_{\text{FC2}}$ can be made sure to be happening only due to the charge exchange process.

## 4. Experiment

Initial calibration of the beam line elements involves optimisation of the performance of CEC and ellipsoid reflector. The calibration of CEC is done with the help of Rb$^+$–Rb charge exchange measurement, while the calibration of the reflector is done by using a fluorescence imaging method. The calibration process is described below.

### 4.1 *Calibration of CEC*

Here we mainly consider the resonant Rb$^+$–Rb charge exchange process responsible for generating the respective atom beam. The resonant interaction [17,19] is

$$\text{Rb}^+(5s) + \text{Rb}(5s) \rightarrow \text{Rb}(5s) + \text{Rb}^+(5s) + \Delta E (= 0). \tag{2}$$
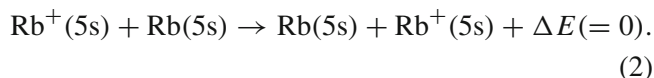
However, there exist small probabilities of other reaction channels where the energy defect ($\Delta E$) is non-zero [17, 19]. This may generate another velocity group of atoms, which differs from the main atomic beam by a very small amount and may result in satellite peaks. However, the presence of other reaction channels can only be verified after analysing the fluorescence spectrum.

The charge exchange is a dynamic process and attenuation of primary ion beam current $I_{\text{FC1}}$ (due to the existence of Rb vapour in CEC) measured on the FC2 may be written as

$$I_{NN} = \eta_T * I_{\text{FC1}} * (1 - \eta) = \eta_T * I_{\text{FC1}} * e^{-n\sigma x}. \tag{3}$$

Here $n$ is the vapour density in the active zone of CEC, $\sigma$ is the cross-section of the reaction and $x$ is the length of active region. At room temperature $I_{NN} \rightarrow \eta_T I_{\text{FC1}}$, i.e. the reading at FC2 before charge conversion takes place and $\eta_T$ is the beam transport efficiency between FC1 and FC2. The value of $n$ may be determined from the ideal gas equation by following the vapour pressure ($P_V$) of the liquid phase for $^{85}$Rb [20]:

$$\log_{10} P_V = 2.881 + 4.312 - \frac{4040}{T}. \tag{4}$$

We considered $^{85}$Rb only as it is the most abundant and stable isotope. In figure 2B we fitted the experimental data by using eqs (3) and (4). Here $\sigma$ is the fitting parameter with a fitted value $\sigma \sim 6.7 * 10^{-15}\,\text{cm}^2$ which matches well with the values mentioned in ref. [21] for a beam energy of 8 keV. However, the main concern is to find out the reservoir temperature where $\eta \propto T$ is valid. This is required to avoid the situation of excess alkali vapour load in CEC leading to multiple scattering of the ion beam and subsequent increment in energy spread, emittance of the beam. We consider a reservoir temperature of 130–150°C (vapour zone temperature $\sim 80$°C–100°C) as the operating condition (the vapour pressure load $=\sim 10^{-3}$ mbar) where even the spectrum of the weakest candidate ($^{87}$Rb $5^2$S$_{1/2}$F $= 1 \rightarrow 5^2$P$_{1/2}$F′) of Rb hyperfine transition manifold is resolved with S/N $\leq 1.5$.

The other part of the CEC calibration involves the consideration of recycling performance of CEC. Following the method of Bacal and Reichelt [16], we estimate $\varphi_C/\varphi_E \approx 0.5(r/l)^2 = 4.6 * 10^{-4}$, where $\varphi_C$ is the flux of the metal atoms directly escaping the hot central region in the solid angle subtended by the cell port and $\varphi_E$ is the total flux leaving the hot central region. Our designed value is almost one order less than that of ref. [16]. To test if $\varphi_C$ is the main factor for the rapid escape of Rb from the CEC, we used 780.033 nm ($\lambda_{air}$) laser beam corresponding to $^{85}$Rb $5S_{1/2} \rightarrow 5P_{3/2}$ transition after turning on the CEC for a few hours (ion beam is absent). No fluorescence is observed outside CEC through side-view ports (see figure 1) by using the infrared (IR) viewer. Also no increase in photon count over background level is noticed. In addition to this, we did not observe any evidence of coating of Rb on the reflector after physically opening the PG section during vacuum maintenance. Hence, the loss of Rb may be expected to be dominated by desorption from cell walls. The ratio $(r/l) \ll 1$ ensures little direct emission from the central region of the charge neutraliser.

### 4.2 *Calibration of the ellipsoidal reflector*

This exercise is carried out to place the PMT at proper position outside the viewport of the photon guide box (figure 3A). For this purpose, we mimic the actual situation of photon–ion beam interaction by applying an absorption imaging method. An Rb vapour cell is inserted within a specially machined PVC tube, where a groove is cut at the cell position (see figure 3B). The PVC tube (with cell) is introduced along the line of the first focus through the holes, which were machined on the surface of the reflector (figure 3B). The reflector (with the cell) is held with a stand and laser beam is passed through the cell.

A bright line of fluorescence is observed with an IR viewer when the laser frequency ($\omega_L$) is tuned to resonance of $^{85}$Rb $^2S_{1/2}$ (F = 3) $\rightarrow$ $^2P_{3/2}$ (F′) absorption. This is similar to the actual beam line situation except the relatively higher scale of fluorescence intensity. The bright spot at the second focal point of the reflector is imaged (figure 3C). When the laser is tuned off-resonance, the fluorescence intensity substantially reduces. This observation is similar to the modelling of the intensity distribution of the reflected light reported in ref. [22]. A histogram of the image spot under on-resonance condition is presented (figure 3D) and it fits well with a Gaussian profile. The FWHM ($\sim$3.5 mm) of the fitted profile indicates that fluorescence of our interest in limited within $\sim\leq$10 mm$^2$ area. So, for a PMT with an active surface of 100 mm$^2$ (current case), proper shielding is required to avoid scattered photons. This test

is conducted outside the beam line for first-hand characterisation of the ellipsoid reflector and to estimate the effective area of the photocathode of PMT illuminated by the photons of our interest. While placing the reflector within the beam line after thorough mechanical alignment, the CLS part is filled with $\sim$1.5 atm of argon gas and laser beam is passed through the first focus. Similar imaging exercise is carried out by using the light scattered from argon but the intensity of the scattered light was not enough to form any image.

### 4.3 *Calibration of PCS*

Here the main task is to optimise the system for measuring fluorescence photons arising from atomic absorption and subsequent spontaneous emission. The raw output from the PMT is observed on an oscilloscope, which shows the nature of photon pulse. The laser intensity is reduced ($\sim\leq$4 mW/cm$^2$) to resolve these pulse trains, i.e. to make the system ready for measuring single photon pulse. In the first run, we used the existing chopped dual gate (A–B) counting set-up [18]. Here A gate of SR400 counts the photons arising from the absorption signal + scattered laser light + background (other than laser) combination whereas the gate B counts background photons (other than laser) only. Hence the output (A–B) gives total photon count due to the absorption signal and scattered laser light. The gate widths and dwell time are adjusted accordingly in SR400. Note here that we used the laser frequency ($\omega_L$) scan for probing the hyperfine transitions. The trigger signal of the laser scan ($\sim$500 s) is used as START/STOP signal of the counter. Initially, the discriminator level is adjusted by directly observing the discriminator output signal peak height on the oscilloscope. The PORT-1 (for X) and D/A (for Y) outputs (typical output ports in SR400) are directly recorded on the oscilloscope. The CEC is now turned on but Doppler-shifted laser frequency ($\omega_L$) (with respect to the velocity of ion beam) is tuned to off-resonance. In this condition, the background photon level is determined which is around $10^4$ photon counts/s (figures 4, 5). Separately, the B gate readout shows $\sim$3 $\times$ 10$^2$ to 5 $\times$ 10$^2$ counts/s due to stray light (other than laser). This indicates that the background count is mainly contributed by the scattered laser light.

It may be noted that the transit time of atoms from the end of CEC to the reflector is $\sim$70$\tau_{5P3/2}$ as per our current design. In such cases, the application of high-frequency modulation of laser intensity to reduce the effect of hyperfine pumping was reported earlier [19, 23]. At present we are constrained with lack of rf driver for the electro-optic modulator and therefore the optical pumping was allowed to happen.
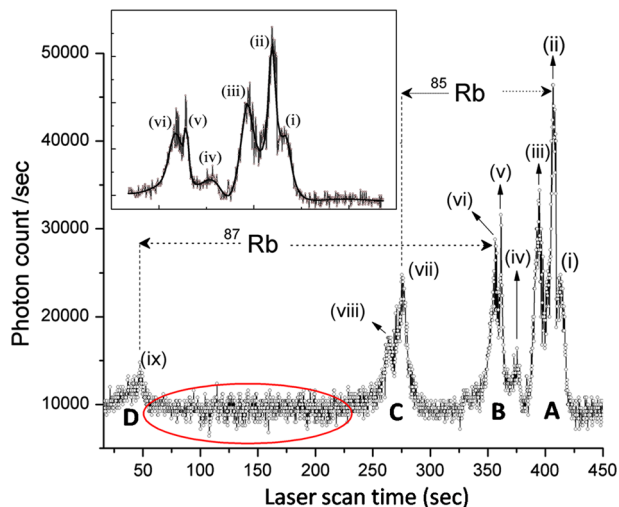
**Figure 4.** Here $^{85}$Rb transitions: (**A**) F = 3 → F′, (**C**) F = 2 → F′; $^{87}$Rb transitions: (**B**) F = 2 → F′, (**D**) F = 1 → F′ are shown under a single laser scan. For this purpose, the dipole magnet setting is switched between $^{85,87}$Rb$^+$ positions. During experiment $I_{FC2}$ readings were ∼70 nA for dipole settings of $^{85}$Rb$^+$($^{87}$Rb$^+$). Peaks (i)→(ix) are clearly discernible. Etalon marker is used to determine laser scan rate, which is used for X-axis calibration. A multipeak pseudo-Voigt fitting (inset) is done to locate the peak positions (see table 1). Fitted values indicate that peaks (iii) and (vi) do not belong to the hyperfine category. These dummy peaks may have appeared due to hysteresis suffered by the dipole magnet during successive switching. The hyperfine components are: (i), (ii) correspond to $^{85}$Rb F = 3 → F′ = 3, 4; (iv), (v) correspond to $^{87}$Rb F = 2 → F′ = 2, 3 (see table 1 for details). Peaks (vii), (ix) indicate transitions: $^{85}$Rb F = 2 → F′, $^{87}$Rb F = 1 → F′. No hyperfine component is observed for these weak transitions. The origin of peak (viii) may be due to hysteresis as mentioned earlier. Further, the highlighted portion (in blue boundary) shows the background of ≤10$^4$ photons/s.

In the present set-up, the laser is scanned to record the fluorescence spectra. To avoid repeatability, single scan recordings are presented in figures 4 and 5. We record the counter D/A output and etalon marker fringes (SA200-5B Thorlabs; F.S.R 1.5 GHz, finesse 233; under static mode) simultaneously to calibrate the X-axis of the laser frequency scan. Apart from this, a wavemeter (Wavemaster; Coherent) is also used for coarse readout of the laser frequency. After the initial calibration, the system is ready for operation. The CEC is turned on and the laser is tuned back to the resonance of Doppler-shifted transition. Initially, the piezovoltage of ECDL is varied manually to see the rise in photon counting on resonance. The fine adjustments of CEC temperature, GATE widths and discriminator voltage are done by observing the variations of count rate in SR400.
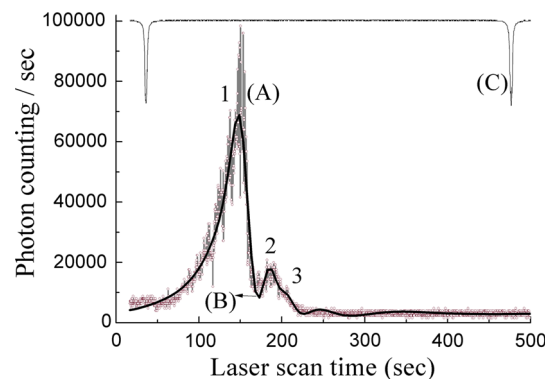


**Figure 5.** The laser scan (A) is zoomed on $^{85}$Rb F = 3 → F′ hyperfine manifold. Peaks 1: F = 3 → F′ = 4 is prominent, 2: F = 3 → F′ = 3 is also identifiable whereas 3: F = 3 → F′ = 2 is barely noticeable. (B) shows etalon fringes used for frequency marking and subsequent X-axis calibration. A multipeak pseudo-Voigt fitting (C) is done to locate the peak positions (see table 2). The fit results are in agreement with the literature values [19].

## 5. Results

The fluorescence spectra of Rb $5^2$S$_{1/2}$ → $5^2$P$_{3/2}$ transition obtained with our system is shown in figure 4. The calculated values of Doppler-shifted laser frequencies for atoms accelerated at 8 keV are 384.056596019 THz ($^{85}$Rb F = 3 → F′), 384.057465116 THz ($^{87}$Rb F = 2 → F′), 384.059509800 THz ($^{85}$Rb F = 2 → F′) and 384.064030229 THz ($^{87}$Rb F = 1 → F′). As per our marking it requires total minimum excursion through 5 FSR of etalon fringes (∼7.5 GHz) to cover all lines of $^{85,87}$Rb isotopes. Figure 4 shows a single scan result where $^{85,87}$Rb transitions are clearly discernible. It may be noted that in our existing ISOL beam line [10] the Danfysik dipole separator (55° bending) resolves the isotopes completely at FC2 (i.e. at the entry of PG section) as verified from the ratio between $I_{FC2}$s under different dipole settings for $^{85,87}$Rb$^+$ ions. Hence, to sample the spectrum (see figure 4) the dipole magnet is manually switched between these settings under a single laser scan. The positions of the resolved spectra (as observed on the wavemeter) are in close proximity with the values previously calculated.

In figure 4 we indicate peaks (i)→(ix) under different transition manifolds. To identify the hyperfine components we used a multipeak pseudo-Voigt fitting (see the inset of figure 4). Fitting of the peaks (i)→(vi) covers the hyperfine transition manifold of $^{85}$Rb F = 3 → F′ and $^{87}$Rb F = 2 → F′. Table 1 shows the values of peak positions. It is found that peak positions (i), (ii) and (iv), (v) are in near accordance with the $^{85}$Rb F = 3 → F′ = 3, 4 and $^{87}$Rb F = 2 → F′ = 2, 3 hyperfine transitions. However, peaks (iii) and (vi) are due to the

change in the magnet settings during the experiment as it is already mentioned that the switching in the settings was necessary to accommodate all the Rb transitions in a single laser scan. During this change, the dipole separator successively selects $^{85,87}$Rb$^+$ beams within a short interval, which gets converted to respective atom beams due to charge exchange. Due to this fact the magnet may possibly get into hysteresis; thereby the resultant dispersion is affected. This could be the reason behind the appearance of the ghost peaks (iii) and (vi). Peaks (vii) and (ix) indicate transitions: $^{85}$Rb F $= 2 \rightarrow$ F′, $^{87}$Rb F $= 1 \rightarrow$ F′. For $^{85}$Rb, the frequency difference between fitted values of the peaks, i.e. (ii)–(iii) and (vii)–(viii) are almost the same. Therefore, the origin of the peak (viii) is also the change in the dipole magnet setting during experiment. The results are included in table 1. Note here that this is unlike the situation mentioned in ref. [24], where the dipole magnet could not completely resolve $^{85,87}$Rb isotopes and a mixed beam was probed.

The *X*-axis of figure 4 is the total scan time. This is calibrated to frequency scale by considering the separation between the first and the last recorded FPI fringes (FSR $\sim$ 1.5 GHz) of the whole laser frequency scan (range $\sim$ 7.5 GHz) as the marker. Simultaneously recorded etalon fringes are shown in figure 5 to highlight the calibration process. The value of the isotope shift extracted from the fitting of the peaks is 139 MHz compared to 78.095 MHz reported in ref. [20]. This deviation is due to the fact that the observed hyperfine peak separations do not exactly match with the literature values [20] and there is a deviation of about 40 MHz. However, when the hyperfine spectrum is recorded only for $^{85}$Rb 5S$_{1/2}$F $= 3 \rightarrow$ 5P$_{3/2}$F′ $- 4, 3, 2$ transitions (figure 5), the difference between the observed and the literature values deceases to about 9 MHz. In this case, the laser is scanned only over $\sim$1.8 GHz which is much smaller compared to the 7.5 GH$z$ scan (figure 4). The deviation is limited to $\sim$0.5% of the total laser frequency scan range for both cases. As the laser frequency is monitored with the help of wavemeter (resolution $= 0.5$ GHz), the above-mentioned deviation cannot be observed directly. The simultaneous recording of the FPI fringes also reveals that the laser frequency scan is not exactly linear over higher scan range. This occurs due to the very slow scan of the laser frequency (2 mHz) by sweeping the piezovoltage over a range of $\pm 10$ V about an offset reference value. The piezotransducer is capacitive in nature. Also the piezo of the laser (Toptica DL100 Pro) is a high voltage (max. 150 V) element. So the mechanical displacement of the piezoelement does not exactly follow the shift in the DC voltage in small steps during the scan if the offset reference is low. For our case (figures 4 and 5) the offset reference is low ($\sim + 20$ V). It seems therefore that the non-linearity in

**Table 1.** Results of multipeak fitting for the data shown in figure 4.

| Peak Nos | Transition manifold (identified from wavemeter reading) | Fitted position of the respective peaks (MHz) | Peak designation | Frequency difference $\Delta$ (MHz) (this work) | Steck data [18] $\Delta$ (MHz) | Remark |
|---|---|---|---|---|---|---|
| (i) | $^{85}$Rb (5S$_{1/2}$F $= 3 \rightarrow$ 5P$_{3/2}$F′) | 7764(6) | F $= 3 \rightarrow$ F′ $= 3$ | (i)–(ii) = 165(6) | 120.640(68) | 40 MHz difference is observed between experimental values and reference value [20]. |
| (ii) | | 7599(0) | F $= 3 \rightarrow$ F′ $= 4$ | (ii)–(iii) = 275(4) | | |
| (iii) | | 7324(4) | | | | |
| (iv) | $^{87}$Rb (5S$_{1/2}$F $= 2 \rightarrow$ 5P$_{3/2}$F′) | 6955(0) | F $= 2 \rightarrow$ F′ $= 2$ | (iv)–(v) = 307(3) | 266.650(9) | |
| (v) | | 6648(3) | F $= 2 \rightarrow$ F′ $= 3$ | (v)–(vi) = 122(7) | | |
| (vi) | | 6526(6) | | | | |

N.B. (I) Peaks (iii) and (vi) do not belong to hyperfine manifolds of $^{85,87}$Rb. This is verified by comparing the wavemeter reading with the calculated values. Further, the nominal laser frequency is scanned High→Low; (iii), (vi) do not match with this direction of scanning. These peaks appear due to the change in dipole magnet settings for $^{85}$Rb and $^{87}$Rb during the experiment (see text for details).
(II) The differences in readings of peak separation between fitted values and ref. [19] arise due to the partial nonlinearity in laser frequency scan (see text for details).

**Table 2.** Results of multipeak fitting for the data shown in figure 5.

| Peak Nos | Transition manifold (identified from wavemeter reading) | Fitted position of the respective peaks (MHz) | Frequency difference $\Delta$ (MHz) (this work) | Steck data [19] (MHz) | Peak designation |
|---|---|---|---|---|---|
| (1) | $^{85}$Rb ($5S_{1/2}F = 3 \rightarrow$ $5P_{3/2}F'$) | 514(1) | (1)–(2) = 112(1) | 120.640(68) | F = 3 → F′ = 4 |
| (2) | | 626(0) | | | F = 3 → F′ = 3 |
| (3) | | 698(1) | (2)–(3) = 72(1) | 63.401(61) | F = 3 → F′ = 2 |

N.B. The differences between the peak separation values between this work and ref. [19] are limited by partial non-linearity of the laser scan. Same etalon calibration (FWHM of the etalon fringe = 6.438 MHz) is used (see figure 5). Under the short-range scan of the laser frequency, the problem of nonlinearity (see table 1) is largely reduced.

the laser scan is mainly responsible for the observed differences in the hyperfine peak separations when the laser frequency was scanned. Further, it may be noted that peaks (ii), (iv) in table 1 and peak 2 in table 2 are assigned with zero statistical uncertainty. These peak frequency values are kept fixed (as per etalon calibration) during fitting process whereas the remaining peak frequencies are kept as floating parameters. This helps in successfully conducting the chi-square fitting process. Identification of different hyperfine components is accomplished through frequency separation values measured from the relative separation of fitted peak positions from the fixed one. As the fixed peak frequency values are already at an offset ($\sim$0.5%) with the actual frequency scale, the fitted peak frequency values also inherit the same systematic deviation.

Figure 5 shows $^{85}$Rb $5^2S_{1/2}$ (F = 3) $\rightarrow$ $5^2P_{3/2}$ (F′ = 4, 3, 2) transitions recorded in a separate scan. The theoretical ratio of hyperfine strengths is $S_{34}:S_{33}:S_{32} \approx$ 1:0.43:0.12 [20]. F = 3 → F′ = 4 is the cyclic transition whereas the other components F = 3 → F′ = 3, 2 have different branching ratios. Here the atoms may decay to F = 2 state, which is outside the optical pumping-decay cycle. Thus, the atoms pumped to F = 2 are lost from the resonance fluorescence process. Due to these reasons, the non-cyclic transitions appear much lower in intensity than their cyclic counterpart. Indeed the transitions F = 3 → F′ = 3 is weak (see figure 5); furthermore the latter one, i.e. F = 3 → F′ = 2 is barely identifiable. The strong asymmetry of the peak, which also limits the peak centre accuracy, may indicate multiple collisions in the CEC generating a tail of slower ions. As we optimised the CEC temperature (see figure 2), the main contribution to this peak asymmetry can be attributed to the dispersion of the original ion beam in and around CEC. Under current configuration, there is no focussing element after the dipole magnet, which may have caused this unwanted outcome. Same multipeak pseudo-Voigt fitting is done on

the F = 3 → F′ manifold (figure 5) and the fitted peak positions are listed in table 2. The experimental FWHMs for individual peaks are about $\sim$80 MHz. This value is much larger than the spontaneous linewidth ($1/\tau_{5P3/2}$) of $5S_{1/2} \rightarrow 5P_{3/2}$ (6 MHz). The linewidth is mainly contributed by the total velocity spread originating from the SI source. Here the calculated spread of ions based on the temperature of the SI source is $\sim$45 MHz. The rest is contributed by the velocity spread of the ions due to potential distribution within the source itself. This gives rise to an additional Doppler broadening, which is $\sim$22 MHz/V in our case. Further, the laser linewidth ($\sim$1 MHz) contributes to the statistical uncertainty factor, which varies within a limit of 7 $\leftrightarrow$ 1 MHz. Rest of the contribution comes from other instrumental broadening, ion-laser beam overlap etc.

The signal detection efficiency of the spectrometer is evaluated from figure 5. The average $^{85}$Rb$^+$ current at FC2 ($I_{FC2}$) is $\sim$70 nA. The charge conversion factor is taken to be $\sim$20% at 80°C of the vapour zone temperature. Also it is a fact that in $^{85}$Rb atom beam, only half of the total atoms are available at F = 3 to participate in optical transition. Hence, the atom flux $N_{atom} \approx I_{FC2}/e * \eta/(1 - \eta) * 0.5 = I_{FC2}/e * 0.25 * 0.5$ is responsible for $^{85}$Rb F = 3 → F′ transition fluorescence. The maximum photon count (photon$_{peak}$) for $^{85}$Rb F = 3 → F′ = 4 (figure 5) transition is $\sim 10^5$/s. We can evaluate a figure of merit of total efficiency ($\epsilon_{total}$) as $\epsilon_{total} = \text{photon}_{peak}/N_{atom} \approx 1/6 * 10^5$, which is the best value obtained under a single scan.

## 6. Conclusion

The CLS facility as a newly added part in the ISOL system at VECC has been described in detail and it is shown that Rb hyperfine levels can be resolved using the same. The sensitivity or signal/noise ratio at present,

although good enough to allow measurements on stable species, needs improvement by two orders of magnitude and more for carrying out studies on beta unstable nuclei. For example, we plan to study radioactive isotopes $^{42,43}$K in the near future that can be produced in our facility with an intensity of $\sim 10^5$ pps [13,14]. We have already figured out the measures to be taken to improve the sensitivity to the desired level. First of all we would be adding additional focussing elements downstream of the dipole magnet to reduce the beam size which is at present about 5 times the laser spot size at the interaction zone. Also, alignment of the laser with respect to the beam would be made better. Instead of scanning the laser, which tends to introduce repeatability problem, scanning of CEC voltage will be introduced by modifying the charge exchange cell appropriately. This would allow repetitive scan and subsequent averaging leading to an improvement in the S/N ratio of the spectrum. Scanning CEC voltage in small steps requires design and fabrication of a new CEC. The new CEC, insulated from the rest of the beamline for floating to a potential of a few kV, is a part of the upgradation plan. It may be noted that in principle the same can be achieved by adjusting the extraction voltage of the ion source but is avoided as each voltage setting needs fresh tuning of all the beamline magnets, which apart from being tedious, introduces the problem of repeatability of beam size, position etc. There is a scope to improve the S/N ratio by reducing stray laser beam scattering by redesigning slits in the beamline around the PG section (particularly holes of the conical light arrester) and properly (optimum) shielding the PMT surface area [22]. Also, we have planned to modify the dipole vacuum chamber to create an opening through which the uninteracted laser photons can pass and be deflected by a mirror, not allowing them to come back. This will considerably improve the background from the scattered laser light. We are currently working on this particular aspect. In addition, the synchronous dual gate photon counting mode needs to be replaced by externally triggered single gate mode operation [25] in order to improve the S/N ratio. The current photon counting system in use is the same one developed by us earlier for experiments related to quantum optics [18]. Though this can extract the Rb hyperfine spectrum, it falls short of achieving high S/N ratio as the present dual get synchronous counting method results in loss of a good fraction of the fluorescence. This will be replaced with externally triggered single gate counting. We are confident that these measures, hardware developments for which are already underway, will improve the signal to noise ratio by much more than two orders of magnitude. Further with the ANURIB project [26] at the beginning stage, the scope of experimenting with truly exotic nuclei using

laser spectroscopy will be within our reach in the near future.

# References

[1] W Demtroeder, *Laserspektroskopie* (Springer Verlag, Berlin, 1993)

[2] S L Kaufman, *Opt. Commun.* **17**, 309 (1976)

[3] W H Wing, G A Ruff, W E Lamb and J J Spezeski, *Phys. Rev. Lett.* **36**, 1488 (1976)

[4] K-R Anton, S L Kaufman, W Klempt, G Moruzzi and R Neugart, *Phys. Rev. Lett.* **40**, 642 (1978)

[5] *Treatise on heavy ion science* edited by D A Bromley (Plenum Press, 1989) Ch. 7, p. 517

[6] R Neugart, *Nucl. Inst. Meas.* **186**, 165 (1981)

[7] H-J Kluge and W Nörtershäuser, *Spectrochim. Acta B* **58**, 1031 (2003)

[8] B Cheal and K T Flanagan, *J. Phys. G* **37**, 113101 (2010)

[9] K P Marinova, *Phys. Part. Nucl.* **35**, 693 (2004)

[10] P Campbell, I D Mooreb and M R Pearson, *Prog. Part. Nucl. Phys.* **86**, 127 (2016)

[11] A Bandyopadhyay, V Naik, D Bhattacharyya, S De Chowdhury, S K Nayak, M Mandal, S Chattopadhyay, A Polly and A Chakrabarti, *Nucl. Insrum. Methods A* **562**, 41 (2006)

[12] J Papuga, M L Bissell, K Kreim, C Barbieri, K Blaum, M De Rydt, T Duguet, , H Heylen, M Kowalska, R Neugart, G Neyens, W Nörtershäuser, M M Rajabali, R Sánchez, N Smirnova, V Somà and D T Yordanov, *Phys. Rev. C* **90**, 034321 (2014)

[13] V Naik, A Chakrabarti, M Bhattacharjee, P Karmakar, A Bandyopadhyay, S Bhattacharjee, S Dechoudhury, M Mondal, H K Pandey, D Lavanyakumar, T K Mandi, D. P Dutta, T Kundu Roy, D Bhowmick, D Sanyal, S C L Srivastava, A Ray and Md S Ali, *Rev. Sci. Instrum.* **84**, 033301 (2013)

[14] Vaishali Naik, Alok Chakrabarti, Mahuwa Bhattacharjee, Prasanta Karmakar, Sampa Bhattacharjee, Arup Bandyopadhyay, Siddhartha Dechoudhury, Dodi Lavanya Kumar, Manas Mondal, H K Pandey, T K Mandi, D P Dutta, Tapatee Kundu Roy, Debasis Bhowmik, Dirtha Sanyal, Ayan Ray, Md Sabir Ali, S C L Srivastava and P Y Nabhiraj, *Nucl. Instrum. Methods B* **317**, 227 (2013)

[15] U Rohrer, PSI graphic transport framework, based on a CERN-SLAC-FERMILAB version by K L Brown *et al*, 2006

[16] M Bacal and W Reichelt, *Rev. Sci. Instrum.* **45**, 769 (1974)

[17] A Klose, K Minamisono, Ch Geppert, N Frömmgenc, M Hammenc, J Kramer, A Krieger, C D P Levy, P F Mantica, W Nörtershäuser and S Vinnikova, *Nucl. Instrum. Methods B* **678**, 114 (2012)

[18] Waseem Raja, Md Sabir Ali, Alok Chakrabarti and Ayan Ray, *Appl. Phys. B* **123**, 202 (2017), https://doi.org/10.1007/s00340-017-6778-8

[19] J F Sell, K Gulyuz and G D Sprouse, *Rev. Sci. Instrum.* **80**, 123108 (2009)

[20] http://steck.us/alkalidata/rubidium85numbers.pdf

[21] J Perel, R H Vernon and H L Daley, *Phys. Rev. A* **138**, 937 (1965)

[22] S Vinnikova, *Development and commissioning of a photon detection system for collinear laser spectroscopy at NSCL*, Masters Thesis (Michigan State University, 2011)

[23] A Voss, M R Pearson, J Billowes, F Buchinger, B Cheal, J E Crawford, A A Kwiatkowski, C D Philip Levy and O Shelbaya, *Phys. Rev. Lett.* **111**, 122501 (2013)

[24] J Krämer, *Construction and commissioning of a collinear laser spectroscopy set-up at TRIGA Mainz*, Ph.D. thesis (Johannes Gutenberg-Universität Mainz, 2010)

[25] http://www.thinksrs.com/downloads/PDFs/Manuals/SR400m.pdf

[26] A Chakrabarti, A Bandyopadhyay, V Naik, S Dechoudhury, M Mondal and P Y Nabhiraj, *Nucl. Instrum. Methods B* **317**, 253 (2013)